

# Unified Radio Interferometric Calibration and Imaging with Joint Uncertainty Quantification

Philipp Arras<sup>1,2,3</sup>, Philipp Frank<sup>1,2</sup>, Reimar Leike<sup>1,2</sup>, Rüdiger Westermann<sup>3</sup>, and Torsten A. Enßlin<sup>1,2</sup>

<sup>1</sup> Max-Planck Institut für Astrophysik, Karl-Schwarzschild-Str. 1, Garching, Germany

<sup>2</sup> Ludwig-Maximilians-Universität München (LMU), Geschwister-Scholl-Platz 1, München, Germany

<sup>3</sup> Technische Universität München (TUM), Boltzmannstr. 3, 85748 Garching, Germany

Received <date>/ Accepted <date>

## ABSTRACT

The data reduction procedure for radio interferometers can be viewed as a combined calibration and imaging problem. We present an algorithm that unifies cross-calibration, self-calibration, and imaging. Being a Bayesian method, that algorithm does not only calculate an estimate of the sky brightness distribution, but also provides an estimate of the joint uncertainty which entails both the uncertainty of the calibration and the one of the actual observation. The algorithm is formulated in the language of information field theory and uses Metric Gaussian Variational Inference (MGVI) as the underlying statistical method. So far only direction-independent antenna-based calibration is considered. This restriction may be released in future work. An implementation of the algorithm is contributed as well.

**Key words.** techniques: interferometric – methods: statistical – methods: data analysis – instrumentation: interferometers

## 1. Introduction

Radio astronomy is on a tear. Super-modern telescopes like MeerKAT, ASKAP, JVLA and ALMA are operating and SKA is in planning. All these telescopes provide high-quality data on an unprecedented scale and much progress is being made instrumental-wise which facilitates enormous improvements in sensitivity and survey speed.

Impressed by these novel facilities the authors of this publication would like to turn attention to the calibration and imaging algorithms that are fed by the data from these telescopes. The amount of scientific insight which can possibly be extracted from a given telescope is limited by the capability of the employed data reduction algorithm. The authors suggest that there is room for improvement regarding the calibration and imaging procedure: the most widely applied algorithms view calibration and imaging as separate problems and are not able to provide uncertainty information. The latter is desperately needed to quantify the level of trust a scientist can put on any result based on radio observations. Furthermore, a statistical sound confrontation of astrophysical models to radio data requires reliable uncertainty quantification. Treating calibration and imaging as separate steps ignores their tight interdependence.

The algorithmic idea presented here is an advancement of the original **RESOLVE** algorithm (**R**adio **E**xtended **S**ources **L**ognormal deconvolution **E**stimator, Junklewitz et al. 2016) and may retain its name. **RESOLVE** is formulated in the language of information field theory (IFT, Enßlin et al. 2009; Enßlin 2018) which is a view on Bayesian statistics applicable wherever (physical) fields are supposed to be inferred. From a Bayesian point of view the question when reducing radio data is the following: Given prior knowledge as well as measurement information about the brightness distribution of a patch of the sky, what is the observers knowledge after having obtained the data? This question is answered by Bayes' theorem in terms of a prob-

ability distribution over all possible sky brightness distributions conditional to the data.

Reconstruction algorithms may be judged based on their statistical integrity or by their performance. The first perspective ultimately leads to pure Bayesian algorithms which are too expensive for typical problems computationally. The latter often leads to ad-hoc algorithms which may perform well in applications but can have major shortcomings like missing uncertainty quantification or negative-flux pixels which is the case e.g. for **CLEAN** (Högbom 1974). **RESOLVE** attempts a compromise between these two objectives. It is based on purely statistical arguments and the necessary operations are approximated such that they can efficiently be implemented on a computer and be used for actual imaging tasks. Thus, the approximations and (prior) assumptions on which **RESOLVE** is based can be written down explicitly.

**RESOLVE** is reasonably fast but cannot compete in pure speed with algorithms like **CLEAN** (Högbom 1974). This is rooted in the fact that **RESOLVE** does not only provide a single sky brightness distribution but needs to update the sky prior probability distribution according to the raw data in order to properly state how much the data has constrained the probability distribution and how much uncertainty is left in the final result. This uncertainty is defined in a fashion such that it can encode the posterior variance and also cross-correlations. Thus, it contains  $O(n^2)$  pieces of information where  $n$  is the number of pixels in the image. Given this massive amount of degrees of freedom it may be surprising that **RESOLVE** is able to return its results after a sensible amount of time. Having said this, there is still potential for improvement. The technical cause for the long runtime is the complexity of the gridding/degridding operation which needs to be called orders of magnitude more often than for conventional algorithms. This problem may be tackled from an information-theoretic perspective in the future.

Turning to the specific subject of the present publication: the data reduction pipeline of modern radio telescopes consists out of numerous steps. In this paper, we would like to focus on the calibration and imaging part. Calibration is necessary because the data is corrupted by a variety of effects including antenna-based, baseline-based and direction-dependent or direction-independent effects (Smirnov 2011). For the scope of this paper only antenna-based calibration terms are considered, a simplification which is sensible for telescopes with a small field of view like ALMA or the VLA. The crucial idea of this paper is to view the amplitude and phase corrections for each antenna as one-dimensional fields which are defined over time. These fields are discretized and regularized by a prior which states that the calibration solution for a given antenna is smooth over time. This removes the ambiguity of an interpolation scheme in between the calibrator observations and the subsequent application of self-calibration. `RESOLVE` being an IFT algorithm, there is no notion of *solution intervals* which are time bins in which traditional calibration algorithms bin the data (see e.g. Kenyon et al. 2018). Instead IFT takes care of a consistent discretisation of the principally continuous fields. Similarly, the sky brightness distribution is defined on a discretized two-dimensional space (only single-channel imaging is performed here).

In practise, the state-of-the-art approach in the IFT community is to define a generative model which turns the degrees of freedom which are learned by the algorithm into synthetic data which can be compared to the actual data in a squared-norm fashion (in the case of additive Gaussian noise). This approach is similar to the so-called RIME (*radio interferometric measurement equation*, Hamaker et al. 1996; Perkins et al. 2015; Smirnov 2011). Therefore, our notation will closely follow the notation defined in Smirnov (2011). Calibration effects which are part of the RIME but left out for simplicity in this publication could in principle be integrated into `RESOLVE`'s framework.

`RESOLVE` may be classified according to the notion of first, second, and third generation calibration established in Noordam & Smirnov (2010): it unifies cross-calibration (1GC), self-calibration (2GC) and imaging. Still it is to be strictly distinguished from existing approaches like Kenyon et al. (2018); Cai et al. (2018); Salvini & Wijnholds (2014) since it focuses on a strict Bayesian treatment combined with consistent discretisation (one of the main benefits of IFT) and does not use computational speed as an argument to drop Bayesian rigidity.

The actual posterior probability distribution of the joint imaging and calibration problem is highly non-Gaussian and therefore not easily storeable on a computer. In order to overcome this apparent problem the posterior is approximated by a multi-variate Gaussian with full covariance matrix. The algorithm prescribes to minimize the *Kullback-Leibler divergence* between the actual posterior and the approximate one which is the information gain between the two probability distributions. The here used variant of this is known as *Metric Gaussian Variational Inference* or MGVI (Knollmüller & Enßlin 2019).

Together with this publication the authors contribute an implementation of `RESOLVE` which is available under the terms of GPLv3.<sup>1</sup> It is based on a library called NIFTY<sup>2</sup>, which is freely available as well.

The paper is divided into four sections. Section 2 discusses the structure of likelihood and prior for the statistical problem at hand. This defines an algorithm which is verified on synthetic

data in Section 3 and afterwards applied to real data from the VLA in Section 4. Section 5 finishes the paper with conclusions and a outlook for future work.

## 2. The Algorithm

### 2.1. Bayes' Theorem

Every reconstruction algorithm needs a prescription of how the quantity of interest  $s$  affects the data  $d$ . This prescription is called *data model*. Combined with statistical information, this model defines the *likelihood*  $\mathcal{P}(d|s)$  which is a probability distribution on data realizations conditioned on a given realization of the signal  $s$ . Bayes' theorem,

$$\mathcal{P}(s|d) = \frac{\mathcal{P}(d|s)\mathcal{P}(s)}{\mathcal{P}(d)}, \quad (1)$$

asks to supplement the likelihood with a *prior probability distribution*  $\mathcal{P}(s)$  which assigns a probability to each signal realization  $s$ . This distribution encodes the knowledge the scientist has prior to looking at the data. Since it is virtually impossible to visualize the *posterior probability distribution*  $\mathcal{P}(s|d)$  in the high dimensional setting of Bayesian image reconstruction one may compute the posterior mean and posterior variance:

$$m := \langle s \rangle_{\mathcal{P}(s|d)} := \int \mathcal{D}s \mathcal{P}(s|d) s, \quad (2)$$

$$\langle |m - s|^2 \rangle_{\mathcal{P}(s|d)} := \int \mathcal{D}s \mathcal{P}(s|d) |m - s|^2. \quad (3)$$

The notation  $\int \mathcal{D}s$  is borrowed from statistical physics and means integrating over all possible configurations  $s$ . For a discussion on this measure in the continuum limit see Enßlin (2018, section 1.8). In practise, this integral is discretized:  $\int \mathcal{D}s = \int \prod_i ds_i$  where  $s_i$  refers to the pixels of the discretized quantity  $s$ .

The term  $\mathcal{P}(d)$  is independent of  $s$  and serves as a normalization factor. It expresses the probability to obtain the data irrespective of what the signal is:  $\mathcal{P}(d) = \int \mathcal{D}s \mathcal{P}(d, s)$ .

In the following the data model and implied likelihood which `RESOLVE` employs is described. This includes the assumptions `RESOLVE` makes about the measurement process. Afterwards, `RESOLVE`'s prior is discussed. For definiteness the notation established in Smirnov (2011) is utilized.

### 2.2. Data Model and Likelihood

The measurement equation of a radio interferometer can be understood as a modified Fourier transform followed by an application of data-corrupting terms, the terms which need to be solved for in the calibration procedure. Assume that the data is only corrupted by so-called *antenna-based direction-independent effects* (DIEs). Then Smirnov (2011, equation 18) reads:

$$V_{pq} = G_p \left( \int \frac{B(l, m)}{n(l, m)} e^{-2\pi i [u_{pq}l + v_{pq}m + w_{pq}(n(l, m) - 1)]} dl dm \right) G_q^\dagger, \quad (4)$$

where:

- $l, m$ : Direction cosines on the sky and  $n(l, m) = \sqrt{1 - l^2 - m^2}$ .
- $p, q \in \{1, \dots, N_a\}$ : Antenna indices where  $N_a$  is the total number of antennas of the interferometer.
- $V_{pq} \in \mathbb{C}^{2 \times 2}$ : Visibility for antenna pair  $(pq)$ .

<sup>1</sup> <https://gitlab.mpcdf.mpg.de/ift/resolve>

<sup>2</sup> Numerical Information Field Theory, <https://gitlab.mpcdf.mpg.de/ift/nifty>

- $(u_{pq}, v_{pq}, w_{pq})$ : Vector which connects antenna  $p$  with antenna  $q$ . The coordinates  $u_{pq}$  and  $v_{pq}$  are aligned with  $l$  and  $m$ , respectively.  $w_{pq}$  is perpendicular to both and points from the interferometer towards the center of the field of view.
- $G_p \in \mathbb{C}^{2 \times 2}$ : Antenna-based direction-independent calibration effect.
- Intrinsic sky brightness in circular basis:

$$B = \begin{pmatrix} I + V & Q + iU \\ Q - iU & I - V \end{pmatrix}, \quad (5)$$

where  $I, Q, U$  and  $V$  are the Stokes parameters (Born & Wolf 1964).

(4) can be understood as a Fourier transform of the sky brightness distribution which is distorted by the terms involving  $n(l, m)$  and corrupted by the calibration terms  $G_p$ . For the purpose of this publication let us rewrite this formula a little: First, only the total intensity  $I$  shall be reconstructed. Second,  $G_p$  is assumed to be diagonal which states that there is no significant polarisation leakage and especially no time-variable leakage. Finally, the temporal structure of the data will be needed for the construction of the prior. Therefore, a time index is added to the above expression:

$$V_{pqt} = G_p(t) \left( \int \frac{B(l, m)}{n(l, m)} e^{-2\pi i [u_{pq}l + v_{pq}m + w_{pq}(n(l, m) - 1)]} dl dm \right) G_q^\dagger(t), \quad (6)$$

where  $G_p(t)$  are diagonal matrices and  $B(l, m)$  is a diagonal matrix which is proportional to unity in polarisation space. Note that  $G_p(t)$  needs to absorb the  $V$ -term from (4) which is possible as long as polarisation leakage is not too time-variable. The  $w$ -term is taken care of by  $w$ -stacking (Offringa et al. 2014) which means that the range of possible values for  $w_{pq}$  is binned linearly such that the integral becomes an ordinary Fourier transform.

Technically, the non-equidistant Fourier transform in (6) is carried out by the NFFT library (Keiner et al. 2009) in our `RESOLVE` implementation.

All in all, (6) prescribes how to simulate data  $V_{pqt}$  given calibration solutions  $G_p(t)$  and an inherent sky brightness distribution  $B(l, m)$  which is what we wanted. In order to declutter the notation in the following let us denote the quantities of interest by  $s = (G_p(t), B(l, m))$  and the map  $R$  such that  $V_{pqt} = R(s)$ .

The commonly used data model is the following:  $d = R(s) + n$ . It assumes additive Gaussian noise (Thompson et al. 1986).<sup>3</sup> Let  $N$  be a diagonal noise covariance matrix with the noise variances on its diagonal and  $\mathcal{G}(s - m, S)$  refers to a Gaussian random field with mean  $m$  and covariance matrix  $S$ . Then, the additive noise can be marginalized over in order to arrive at an expression for the likelihood:

$$\mathcal{P}(d|s) = \int \mathcal{D}n \mathcal{P}(d|s, n) \mathcal{P}(n) \quad (7)$$

$$= \int \mathcal{D}n \delta(n - (d - R(s))) \mathcal{G}(n, N) \quad (8)$$

$$= \mathcal{G}(d - R(s), N). \quad (9)$$

The likelihood distribution  $\mathcal{P}(d|s)$  contains all information about the measurement device and the measurement process which the inference algorithm will take into account.

<sup>3</sup> In fact, all noise which stems from the antenna electronics is not independent since it speaks into all visibilities which involve this antenna due to the correlation procedure. The correct choice for the likelihood may be an Inverse Complex Wishart distribution that being used would add complexity to the problem which is outside the scope of this paper.

Let us conclude the discussion on data and likelihood with three remarks: First, the likelihood does not depend on the statistical method at hand. All simplifications being made are rooted in practical reasons in the implementation process. There is no fundamental reason in not taking e.g. a more accurate noise model or a more sophisticated calibration structure into account.

Second, the employed notation already hints at the goal of describing an algorithm which jointly calibrates and images: the generalized response function  $R$  takes at the same time the calibration parameters  $G_p(t)$  and the intrinsic sky brightness distribution  $B$  as an argument.

Finally, consider what happens if the telescope alternates between observing the science target and observing a calibration source. Then, both the data set and the intrinsic sky brightness consists out of two parts and the likelihood separates:

$$\mathcal{P}(d|s) = \mathcal{P}(d_c|s) \mathcal{P}(d_s|s) \quad (10)$$

From the likelihood perspective calibration and science source are two separate things. However, as soon as the one-dimensional calibration fields are supplemented by a prior which imposes temporal smoothness the degrees of freedom regarding the science target and the calibration target interact. This is going to solve the problem of applying interpolated calibration solutions in traditional cross-calibration in a natural way.

### 2.3. Prior

Let us turn to the prior probability distribution. Contrarily to the widespread opinion that the prior is arbitrary and biases the result, the `RESOLVE` prior will be deduced from a definite set of assumptions of which some are indisputable and others may be debated. Note that the technical framework in which `RESOLVE` is implemented allows for a variety of different priors which may supersede the one presented in this paper.

As stated before  $G_p(t)$  are assumed to be diagonal:

$$G_p(t) = \begin{pmatrix} g_p^{(0)}(t) & 0 \\ 0 & g_p^{(1)}(t) \end{pmatrix}. \quad (11)$$

The elements of this matrix are functions defined over time and take complex non-zero values:<sup>4</sup>

$$g_p^{(i)} : [t_0, t_1] \rightarrow \mathbb{C}^*, \quad i \in \{0, 1\}, p \in \{1, \dots, N_a\}. \quad (12)$$

The natural way of parameterizing a function taking values in  $\mathbb{C}^*$  is in polar coordinates:

$$g_p^{(i)}(t) = \exp(\lambda_p^{(i)}(t) + i\phi_p^{(i)}(t)), \quad (13)$$

where  $\lambda_p^{(i)} : [t_0, t_1] \rightarrow \mathbb{R}$  and  $\phi_p^{(i)} : [t_0, t_1] \rightarrow \mathbb{R}/2\pi\mathbb{Z}$ . The modulus and the phase of the complex gains  $g_p^{(i)}$  have different physical origins: the modulus describes a varying amplification of the signal in the antenna electronics which is rooted amongst others in varying temperature of the receiver system. Varying phases stem from fluctuations in the atmosphere. Therefore, these two ingredients of  $g_p$  have differing typical timescales a priori.

The prior knowledge on  $\lambda_p^{(i)}$  and  $\phi_p^{(i)}$  is the following:  $\{\lambda_p^{(i)}\}, \{\phi_p^{(i)}\}$ , respectively, share a typical behaviour over time for all antennas  $p$ , both of which are not known a priori and need to be inferred from the data as well. This typical behaviour does not change over time. Additionally, all  $\lambda_p^{(i)}, \phi_p^{(i)}$  evolve smoothly over

<sup>4</sup>  $\mathbb{C}^*$  are the units of  $\mathbb{C}$ , i.e.  $\mathbb{C}^* := \mathbb{C} \setminus \{0\}$ .

time. Mathematically, this can be captured by Gaussian random fields:

$$\mathcal{P}\left(\left(\lambda_p^{(i)}, \phi_p^{(i)}\right)_{i,p} \mid \Lambda, \Phi\right) = \prod_{i,p} \mathcal{G}\left(\lambda_p^{(i)}, \Lambda\right) \mathcal{G}\left(\phi_p^{(i)}, \Phi\right), \quad (14)$$

with  $\Lambda, \Phi$  defined such that the Gaussian random fields obey homogeneous but still specifically unknown statistics. This means that not only the calibration solutions themselves but also their prior correlation structure is going to be inferred. For this a prior on the covariances needs to be supplemented:  $\mathcal{P}(\Lambda), \mathcal{P}(\Phi)$ . How to set up the prior on  $\Lambda$  and  $\Phi$  such that they implement homogeneous statistics and which parameters they take is described in Section 2.4.

Let us turn to the prior on the sky brightness distribution  $B(l, m)$ . Recall that the matrix  $B(l, m)$  is assumed to be diagonal and proportional to unity:

$$B(l, m) = \begin{pmatrix} b(l, m) & 0 \\ 0 & b(l, m) \end{pmatrix}, \quad (15)$$

with  $b(l, m) : [l_{\min}, l_{\max}] \times [m_{\min}, m_{\max}] \rightarrow \mathbb{R}_{>0}$  mapping the field of view to the set of positive real numbers since sky brightness is inherently a positive quantity.<sup>5</sup> For the scope of this publication, the sky brightness contains only a diffuse component. It shall be modeled similarly to the modulus of the calibration terms: it is strictly positive a priori, smooth over its domain and may vary over large scales. Therefore, define  $b(l, m) = e^{\psi(l, m)}$  and let  $\psi(l, m)$  be a two-dimensional Gaussian random field with correlation structure  $\Psi$  which is going to be inferred as well:

$$\mathcal{P}(\psi \mid \Psi) = \mathcal{G}(\psi, \Psi). \quad (16)$$

All in all, the basic structure of the priors on all terms appearing in (6) has been described apart from the construction of the prior on all covariance matrices which is the objective for the next section.

## 2.4. Correlated Fields

To account for correlations of a Gaussian distributed field  $\psi$  the following statements are assumed to be true:

1. The autocorrelation of  $\psi$  can be characterized by a power spectrum  $P_\Psi(|k|)$ , where  $k$  is the coordinate of the Fourier transformed field.
2. The power spectrum  $P_\Psi(|k|)$  is a positive quantity that can vary over many orders of magnitudes.
3. Physical power spectra are falling with  $|k|$ , typically according to a power law.
4. Given enough data, it shall be possible to infer any kind of differentiable power spectrum.

Note that the first assumption is equivalent to the seemingly weaker assumptions:

- In absence of data, there is no special direction in space or time, i.e. a-priori the correlation of the field is invariant under rotations.
- In absence of data, there is no special point in space or time, i.e. a-priori the correlation of field values is invariant under shifts in space or time.

<sup>5</sup> Note the reference to Högbom's CLEAN which has positivity not build in (Högbom 1974).

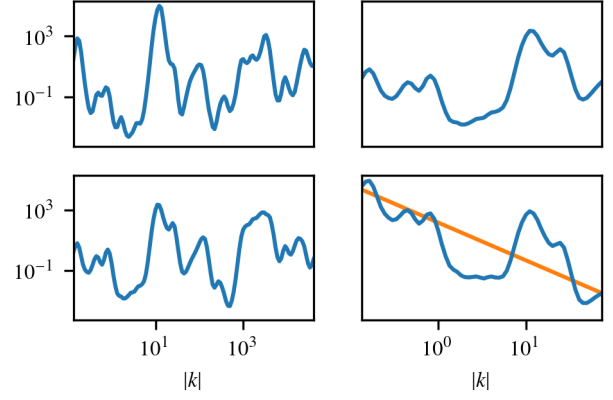


**Fig. 1.** Steps of the generative process defined in Eq. (17). *Top-left:* Smooth, periodic field defined on the interval  $[t_0, 2t_1 - t_0]$ . *Bottom-left:* (anti-)symmetrized version of the above. *Top-right:* Projection of the symmetrized field to half of the original domain  $[t_0, t_1]$ . *Bottom-right:* Resulting double logarithmic amplitude spectrum after addition of the power-law (orange) to the above.

This equivalence is called *Wiener-Khinchin theorem* (Wiener 1949; Khintchin 1934).

It is assumed that  $\psi$  as well as its power spectrum  $P_\Psi(|k|)$  are unknown. Therefore, both need a prior which may be formulated as generative model: an operator that generates samples for  $\psi$  and its square root power spectrum (henceforth called *amplitude spectrum*) from one or multiple white Gaussian fields. Formulating a prior as generative model has several theoretical and practical advantages (Knollmüller & Enßlin 2018).

We propose the following ansatz for an operator that converts independent normal distributed fields,  $\phi$  and  $\tau$  to the amplitude spectrum of the correlated field  $\psi$ . This operator is called *amplitude operator*  $A_C$  (see Figure 1 for an illustrative example):

$$A_C(\tau, \phi) = (\text{Exp}^* \text{Exp}) \left( 0.5 \cdot \left[ \log(k) (\sigma_m \tau_m + \bar{m}) + \sigma_{y_0} \tau_{y_0} + \bar{y}_0 + (\text{sym} \circ \tilde{\mathcal{F}}_{\log(k)t}) (\text{cp}(t) \cdot \phi(t)) \right] \right), \quad (17)$$

where  $C = (a, t_0, \bar{m}, \bar{y}_0, \sigma_m, \sigma_{y_0}, \alpha, \beta)$  denotes the tuple of parameters (all real numbers),  $\text{Exp}^*$  denotes the pullback of a field by the exponential function acting on  $\log(|k|)$ <sup>6</sup>,  $\text{Exp}$  denotes exponentiation of the field values,  $\tilde{\mathcal{F}}_{\log(k)t}$  denotes the Fourier transform of a space with coordinates  $t$  to the logarithmic coordinates  $\log(k)$  of the power spectrum,  $\bar{m}$  and  $\bar{y}_0$  are the slope and the  $y$ -intercept of the a-priori mean power law,  $\text{sym}$  is an (anti-)symmetrizing operation defined to operate on a field  $\phi$  over the interval  $[t_0, t_1]$  as:

$$2 \cdot \text{sym}(\phi)(x) = \phi(x) - \phi(2t_1 - t_0 - x), \quad (18)$$

for  $x \in (t_0, 2t_1 - t_0)$ . In words,  $\text{sym}$  mirrors the field and subtracts it from itself, then restricts the domain to half the original size. Finally,  $\text{cp}$  is the log-cepstrum:

$$\text{cp}(t) = a \cdot \left( 1 + (t/t_0)^{-2} \right). \quad (19)$$

<sup>6</sup> Let  $\phi : U \rightarrow V$  with  $U, V \subseteq \mathbb{R}$  open and  $f : V \rightarrow \mathbb{R}$  a smooth function, i.e. a field. Then  $(\phi^* f)(t) := f(\phi(t))$  denotes the pullback of  $f$  by  $\phi$ . In other words: the field  $f$  is transformed to a different coordinate system whose coordinates are related to the original one by  $\phi$ .

Let us show that (17) meets the above requirements. Requirement 1 is trivial. Requirement 2 is met since the amplitude spectrum is constructed by applying an exponential function to a Gaussian field. Thus, all values are positive and can vary over several orders of magnitudes.

To requirement 3: In absence of data, the mean of the inferred white fields  $\phi$  and  $\tau$ , to which the amplitude operator is applied, will remain zero. For  $\phi = 0$  and  $\tau = 0$ , (17) becomes:

$$(\text{Exp}^* \text{Exp})(0.5 \cdot [\bar{m} \log(k) + \bar{y}_0]), \quad (20)$$

which is the equation for a power law with spectral index  $\bar{m}$ . A preference for falling spectra can be encoded by choosing the hyperparameter  $\bar{m}$  to be negative.

To requirement 4: Let us show that any differentiable function lies in the image space of the amplitude operator. This implies that any differentiable amplitude spectrum can be inferred given enough data. Let  $\phi$  be an arbitrary smooth field over the interval  $[t_0, t_1]$  and  $\phi_{\text{sym}}$  be a smooth field which has a point symmetry at  $(t_1, \phi(t_1))$  and is defined on the interval  $[t_0, 2t_1 - t_0]$ :

$$\phi_{\text{sym}}(t) = \begin{cases} \phi(t) & \text{for } t \in [t_0, t_1], \\ 2\phi(t_1) - \phi(2t_1 - t) & \text{for } t \in (t_1, 2t_1 - t_0]. \end{cases} \quad (21)$$

$\phi_{\text{sym}}$  is a continuous and differentiable continuation of  $\phi$  at  $t_1$ . Let us decompose  $\phi_{\text{sym}}$  into a linear part and a residual term:

$$\phi_{\text{sym}}(t) = m \cdot (t - t_0) + y_0 + \phi_{\text{res}}(t), \quad (22)$$

with:

$$y_0 = \phi_{\text{sym}}(t_0), \quad (23)$$

$$m = \frac{\phi_{\text{sym}}(2t_1 - t_0) - \phi_{\text{sym}}(t_0)}{2(t_1 - t_0)}, \quad (24)$$

$$\phi_{\text{res}}(t) = -m \cdot (t - t_0) - y_0 + \phi_{\text{sym}}(t). \quad (25)$$

The residual term is a differentiable periodic function:

$$\begin{aligned} \phi_{\text{res}}(t_0) &= \phi_{\text{res}}(2t_1 + t_0) \\ \Leftrightarrow \phi_{\text{sym}}(t_0) - \phi_{\text{sym}}(t_0) &= -\phi_{\text{sym}}(2t_1 - t_0) + \phi_{\text{sym}}(t_0) \\ &\quad - \phi_{\text{sym}}(t_0) + \phi_{\text{sym}}(2t_1 + t_0) \end{aligned} \quad (26)$$

$$\begin{aligned} \phi'_{\text{res}}(t_0) &= \phi'_{\text{res}}(2t_1 + t_0) \\ \Leftrightarrow \phi'(t_0) - m &= \phi'_{\text{sym}}(2t_1 + t_0) - m \\ \Leftrightarrow \phi'(t_0) - m &= \phi'(t_0) - m \end{aligned} \quad (27)$$

Thus,  $\phi_{\text{res}}$  can be represented in Fourier space by a field that falls off at least with second order. This is exactly how  $\phi_{\text{res}}$  is represented in (17). Assuming that the mean and the slope of the linear part is well-represented by its prior distribution, it is indeed possible to represent any kind of differentiable amplitude spectrum. All in all, all four requirements are met by (17).

There remains one unconstrained degree of freedom, the value of the power spectrum at  $|k| = 0$ , the *zero-mode*. As the zero-mode describes the magnitude of the overall logarithmic flux, it is decoupled from the remaining spectrum and should have its own prior. This value is fixed by imposing an inverse gamma prior on the zero-mode, which restricts it to be a positive quantity, while still allowing for large deviations.

To sum up, the amplitude operator depends on eight hyperparameters:

- $a, t_0$ : The amplitude parameter and the cutoff scale of the log-cepstrum.
- $\bar{m}, \bar{y}_0$ : The prior means for the slope and the height of the power law.

- $\sigma_m, \sigma_{y_0}$ : Corresponding standard deviations.
- $\alpha, \beta$ : Shape and scale parameter of the inverse gamma prior for the zero-mode.

Note that the assumptions made at the beginning of the section apply to a wide variety of processes, regardless of their dimensionality. This generic correlated field model has already been successfully used in a number of synthetic and real applications (Leike & Enßlin 2019; Knollmüller & Enßlin 2018, 2019; Knollmüller et al. 2018; Hutschenreuter & Enßlin 2019). In *RESOLVE*, the amplitude operator is used as a prior for the amplitude spectra of the antenna calibration fields and the image itself.

## 2.5. The Full Algorithm

In the foregoing sections, the full likelihood and prior is described. Now, all ingredients shall be stacked together to build the full algorithm. Let us assume that the data set consists out of two alternating observations: observations of a calibrator source and observations of the science target. This means that the likelihood splits into two parts as indicated in (10). In contrast to the sky brightness distribution of the science target the one of the calibrator  $B_c$  is known: it is a point source in the middle of the field of view. The one of the science target shall be reconstructed.

The full likelihood takes the form:

$$\mathcal{P}(d_t|\xi)\mathcal{P}(d_c|\xi) = \prod_{a \in \{t,c\}} \mathcal{G}(d_a - R_a(\{G_p^{(i)}\}, B_a), N_a \otimes \mathbf{1}), \quad (28)$$

$$B_t = \exp \circ \mathcal{F} \circ (\xi_B \cdot A^B), \quad (29)$$

$$G_p^{(i)} = \begin{pmatrix} g_p^{(i)} & 0 \\ 0 & g_p^{(i)} \end{pmatrix}, \quad (30)$$

$$g_p^{(j)} = \exp(\lambda_p^{(j)} + i\phi_p^{(j)}), \quad (31)$$

$$\lambda_p^{(i)} = Z \circ \mathcal{F} \circ (\xi_{\lambda_p^{(i)}} \cdot A^\lambda), \quad (32)$$

$$\phi_p^{(i)} = Z \circ \mathcal{F} \circ (\xi_{\phi_p^{(i)}} \cdot A^\phi), \quad (33)$$

$$A^B = A_{C_B}(\xi_{A_B}), \quad (34)$$

$$A^\lambda = A_{C_\lambda}(\xi_{A_\lambda}), \quad (35)$$

$$A^\phi = A_{C_\phi}(\xi_{A_\phi}). \quad (36)$$

where  $C_x$  denote the tuple of parameters of the respective amplitude operator,  $Z$  is a padding operator. The unit matrices in (28) is a  $2 \times 2$  matrix similar to the matrix in (5). The tuple of all excitation fields is called  $\xi$ :

$$\xi = \left( \xi_B, \xi_{A_B}, \xi_{A_\lambda}, \xi_{A_\phi}, \xi_{\lambda_0^{(0)}}, \dots, \xi_{\lambda_{N_a}^{(1)}}, \xi_{\phi_0^{(0)}}, \dots, \xi_{\phi_{N_a}^{(1)}} \right). \quad (37)$$

As discussed before this model is set up such that the excitation fields  $\xi$  have white Gaussian statistics a priori:

$$\mathcal{P}(\xi) = \mathcal{G}(\xi, \mathbf{1}). \quad (38)$$

The posterior probability distribution is given by:

$$\mathcal{P}(\xi|d_t, d_c) \propto \mathcal{P}(d_t, d_c, \xi) = \mathcal{P}(d_t|\xi)\mathcal{P}(d_c|\xi)\mathcal{P}(\xi). \quad (39)$$

Finally, the statistical model which shall be employed in this publication is fully defined.

## 2.6. Inference Algorithm

The probability distribution (39) has too many degrees of freedom in order to be represented on a computer. RESOLVE solves this problem by approximating this full posterior distribution by a multivariate Gaussian distribution whose covariance is equated with the inverse Fisher information metric. The latter can be represented symbolically alleviating the need for an explicit storage and handling of otherwise prohibitively large matrices. This algorithm is called *Metric Gaussian Variational Inference* (MGVI) and is described in full length in Knollmüller & Enßlin (2019) and implemented in NIFTY.<sup>7</sup> The following is a non-exhausting outline of Knollmüller & Enßlin (2019).

MGVI means to minimize the Kullback-Leibler (KL) divergence<sup>8</sup> between the actual posterior and the approximate one:

$$\text{KL}(\mathcal{P}_1 \parallel \mathcal{P}_2) = \int \mathcal{D}s \mathcal{P}_1(s) \log \left( \frac{\mathcal{P}_1(s)}{\mathcal{P}_2(s)} \right), \quad (40)$$

where  $\mathcal{P}_1$  is more informed compared to  $\mathcal{P}_2$ . However, it is apparent that it is virtually impossible to perform the integration with respect to the posterior distribution as integration measure. Therefore, MGVI exchanges the order of the arguments of the KL divergence such that the integral can be approximated by samples of the approximate posterior:

$$F[\xi] = \langle \mathcal{H}(\xi + x, d) \rangle_{x \sim \mathcal{G}(x, D(\xi))}, \quad (41)$$

where  $\mathcal{H}(\xi, d) := -\log \mathcal{P}(\xi, d)$  is the information Hamiltonian and  $D(\xi)$  the Fisher information.  $F[\xi]$  is a cost function which can be minimized with respect to  $\xi$ . Suitable (2nd order) minimizers are provided by NIFTY.

With the help of the above approximation scheme one gets a computational handle on the posterior. The drawbacks of this approach include: It systematically underestimates the variance of the posterior and it is not suited for extremely non-Gaussian and especially multi-modal probability distributions. Nonetheless, it is able to capture very non-trivial correlation structures since it takes the Fisher information into account.

Note that nothing like complex Wirtinger derivatives which are central to CUBICAL, another modern calibration algorithm (Wirtinger 1927; Kenyon et al. 2018), are needed since all inferred fields  $\xi$  are real.

## 3. Verification on Synthetic Data

This section is devoted to the verification of the algorithm, i.e. the reconstruction of a synthetic sky brightness distribution from a simulated observation and artificial noise. The set-up is described followed by a comparison of the ground truth and the reconstruction. Application to real data, where not modelled effects may occur and the ground truth is unknown, is presented in Section 4.

Let us employ a realistic uv-coverage<sup>9</sup> (see Figure 2). As synthetic sky brightness distribution the field displayed in Figure 3 is used. It is a random sample assuming the power spectrum displayed in orange in Figure 4. The noise-less simulated visibilities are corrupted by noise whose level is visualized in Figure 5. The resulting information source, i.e. the naturally weighted dirty image, is shown in Figure 6.

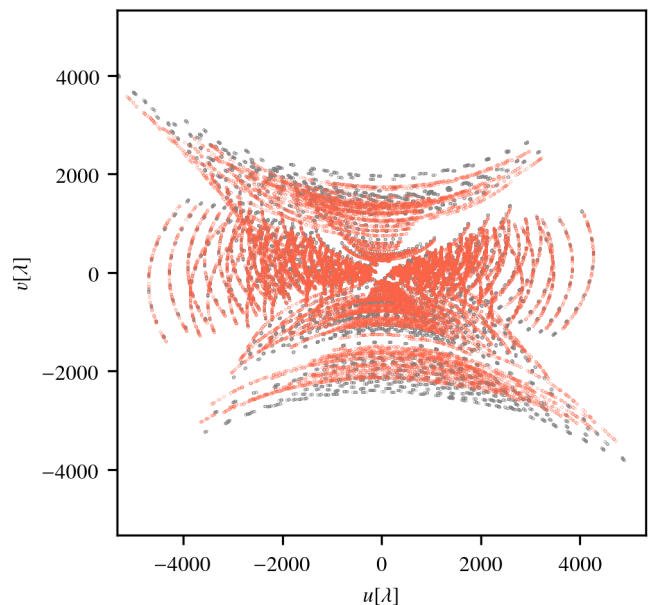


**Fig. 2.** Random sample (30000 points) of uv-coverage of a G327.6+14.6 (SN1006) observation with VLA. The gray and red points indicate the uv coverage of the calibration source and the science target, respectively.

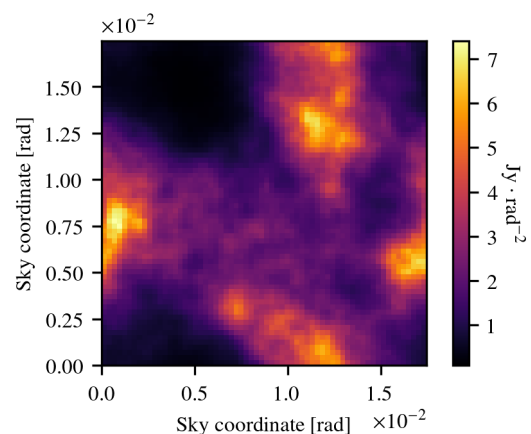


**Fig. 3.** Synthetic observation: Ground truth sky brightness distribution  $b(l, m)$  with  $60'$  field of view.

This synthetic observation is set up in a fashion such that the calibration artifacts are stronger and the noise level is higher as compared to real data (see Section 4) in order to demonstrate RESOLVE's capabilities in bad data situations. The calibration artifacts which have been applied are visualized in Figure 7.

RESOLVE is run on this synthetic data in order to compare its output and uncertainty estimation to the (known) ground truth. The prior parameters are listed in Table 1. Additionally, we choose a resolution of  $64^2$  pixels for the sky brightness distribution with a field of view of  $60'$  and 256 pixels for the calibration fields which are defined on a temporal domain. As the total length of the observation was  $\sim 220$  min one temporal pixel is  $\sim 50$  s long. These temporal pixels shall not be confused with solution intervals of traditional calibration schemes where the data is binned on a grid and then the calibration parameters are solved for. In IFT fields are by their nature continuous quantities which are discretized on an arbitrary grid. For convenience a regular

<sup>7</sup> <https://gitlab.mpcdf.mpg.de/ift/nifty>

<sup>8</sup> Also known as *discrimination information*.

<sup>9</sup> VLA archive project code: AM0754, Jan 24, 2003, L-Band 1369.95 MHz.

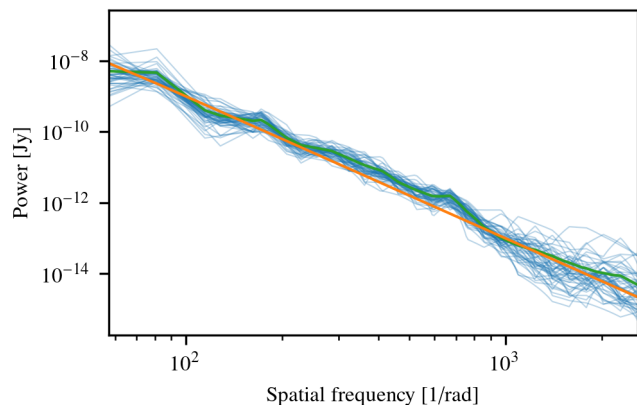


**Fig. 4.** Synthetic observation: Power spectrum of log-sky brightness distribution. orange: ground truth, green: posterior mean, blue: posterior samples.

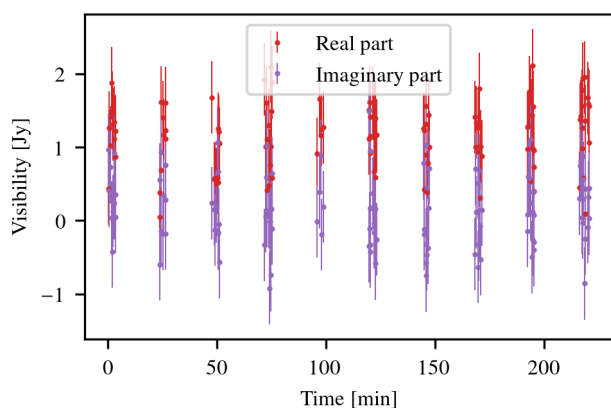


**Fig. 5.** Synthetic observation: Visibilities of calibrator observation (polarisation L, only visibilities of antennas 1 and 3). Thus, a constant value of  $1 + 0j$  Jy is expected. All deviations from this are either noise or calibration errors. The error bars show the standard deviation on the data points.

	$a$	$t_0$	$\bar{m}$	$\bar{y}$	$\sigma_m$	$\sigma_{y_0}$	$\alpha$	$\beta$
$A$	2	2	-4	5	1	3	4	$5 \cdot 10^{-3}$
$\lambda$	1.5	1	-4	-37	0.5	1	2	20
$\phi$	1.5	1	-4	-36	0.5	1	2	20

**Table 1.** Synthetic observation: Prior parameters.

grid was chosen. Then the data provides information on each pixel which is propagated to the neighbouring pixels through the prior (the calibration fields are assumed to be smooth over time). Therefore, the user is free to choose the resolution of the fields in IFT algorithms as long as it is finer than the finest structure which shall be reconstructed.

Let us turn attention to the results. As pointed out `RESOLVE` is a Bayesian algorithm whose output is not a single image of the observed patch of the sky but rather a probability distribution of all possible sky configurations. The MGVI algorithm approximates this non-Gaussian probability distribution with a Gaussian in the space of  $\xi$ , i.e. the eigenspace of the prior covariance. This implies again non-Gaussian statistics on quantities like  $b(l, m)$ ,  $\lambda_p^{(i)}$  and  $\phi_p^{(i)}$  since they depend in a non-linear fashion on  $\xi$ . The only useful way to visualize this probability distribution is to analyze

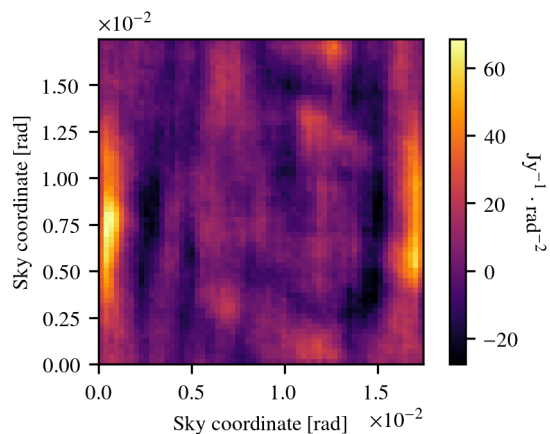


**Fig. 6.** Synthetic observation: Information source  $j = R_i^T N_i^{-1} d_i$ .

a finite number of samples from it which `RESOLVE` can generate. A given set of samples can then be analyzed with standard statistical means like the pixel-wise mean and variance.

Figures 8, 9, 10, 11 show the posterior mean, the absolute value of the residual, the standard deviation of the sky brightness distribution and the residual divided by the standard deviation, respectively, computed from 100 posterior samples. The algorithm has managed to correctly perform the calibration and to reconstruct the sky brightness distribution. The structures on small scales of the ground truth (Fig. 3) could not be recovered due to the noise on the synthetic measurement. Remarkably, the proposed uncertainty is a bit too small compared to the residuals. In particular, 44.2%, 72.8%, 88.7% of the pixels lie within  $1\sigma$ ,  $2\sigma$ ,  $3\sigma$ , respectively. Clearly, this is rooted in the fact that the posterior on the sky brightness is not only non-Gaussian but also highly correlated. Figure 11 illustrates this:  $5\sigma$  errors are more common than a corresponding Gaussian statistics would suggest and maybe more strikingly the errors exhibit a spacial correlation structure. Therefore, a pixel-wise standard deviation does not capture the full complexity of the posterior distribution. Nonetheless, one may always remember that uncertainties are underestimated by MGVI as discussed before.

Since `RESOLVE` does not assume a specific power spectrum as prior for the reconstruction but rather learns it together with the sky brightness from the data, `RESOLVE` also provides the user uncertainty on the power spectrum: see Figure 4. Note that the posterior variance on the power spectrum increases towards the boundaries of the plot. This is because interferometers do not provide information on scales larger than the ones which belong to the shortest baseline. On small scales an interferometer is limited by the noise level which leads to an increased variance in the power spectrum on the right-hand side of the plot.

Next, let us turn to the calibration solutions. Figure 7 shows a comparison of the ground truth and the posterior provided by `RESOLVE`. Since two polarisations are considered (LL and RR) for both the amplitude and the phase of the antenna-based calibration term, Figure 7 has four rows. On first sight, the posterior mean and the ground truth are indistinguishable by eye and the residuals and posterior standard deviation fit together nicely. There is a significant increase of the uncertainty for e.g. antenna 2 towards the end of the observation. The reason for this lies in the fact that a flagged data set was used and that simply all data points involving this antenna have been flagged from the beginning of the observation up to  $\sim 2$ h.

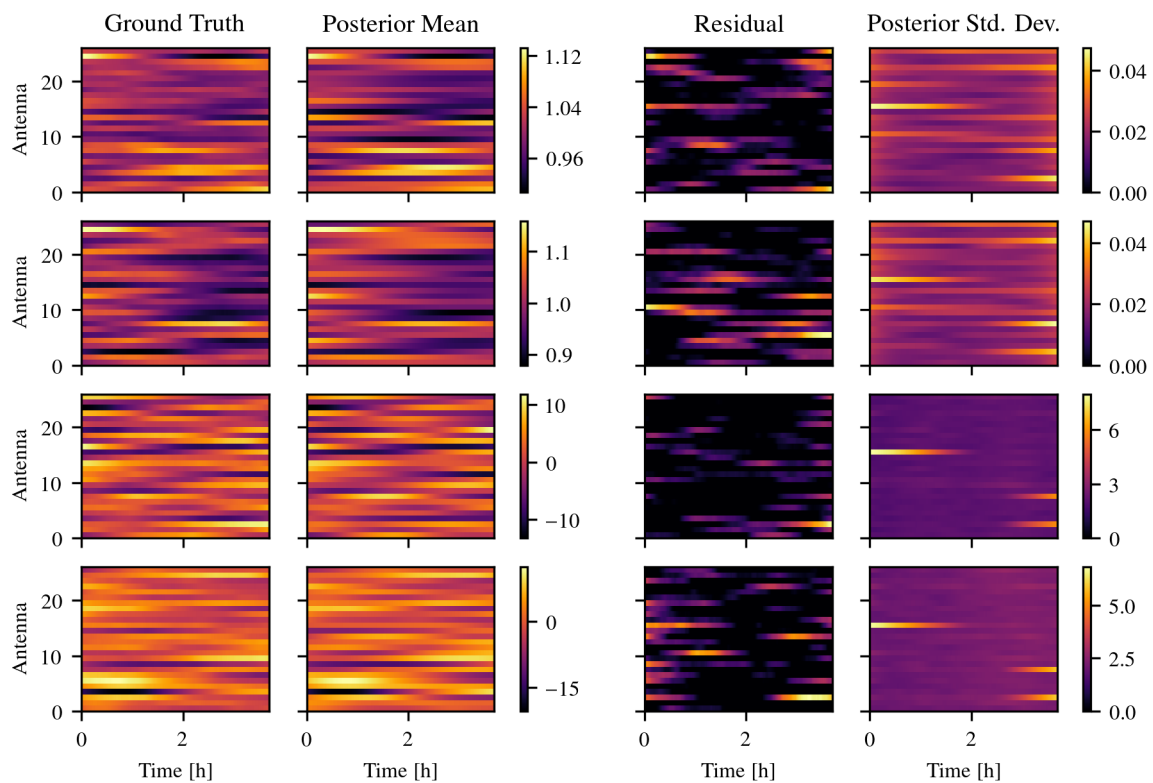


**Fig. 7.** Synthetic observation: Calibration solutions. The first two rows show the amplitude and the lower two rows show the phase calibration solutions. The first and the third row refer to LL-polarisation and the second and last row to RR-polarisation. The third column shows the absolute value of the difference between posterior mean and ground truth. The fourth column displays the point-wise posterior standard deviation as provided by RESOLVE. Amplitudes do not have a unit as they are a simple factor applied to the data. Phases are shown in degrees.

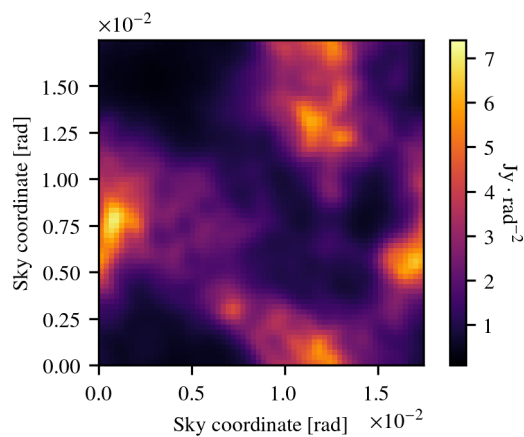


**Fig. 8.** Synthetic observation: posterior mean of sky brightness distribution  $b(l, m)$ .

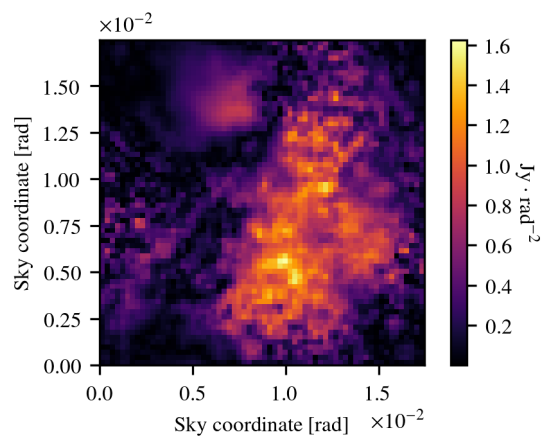


**Fig. 9.** Synthetic observation: absolute value of the difference between ground truth and posterior mean.

To illustrate this more explicitly, Figures 12 and 13 display the calibration solution for one antenna respectively. The ground truth lies within the bounds of uncertainty indicated by the samples. Note that all data points have been flagged on the left-hand side of Figure 12. Since no information about the phase is available here the only constraint is the prior which enforces temporal smoothness. Consistently, the uncertainty increases where no information is available.

Finally, let us demonstrate what kind of other information posterior samples can reveal. Say, a scientist is interested in the integrated flux over a certain region. In addition to the image,

this integrated flux comes with an uncertainty which can be calculated by averaging over posterior samples of the sky brightness distribution. An example is shown in Figure 14. The scatter of the histogram is caused by the noise influence on the data, the (un)certainty of the calibration solutions, and ultimately the uv-coverage. The authors are not aware of any other radio aperture synthesis algorithm which is able to provide this kind of probabilistic posterior information.

All in all, the proposed method is able to recover the ground truth and is able to supplement it with an appropriate uncertainty estimation.



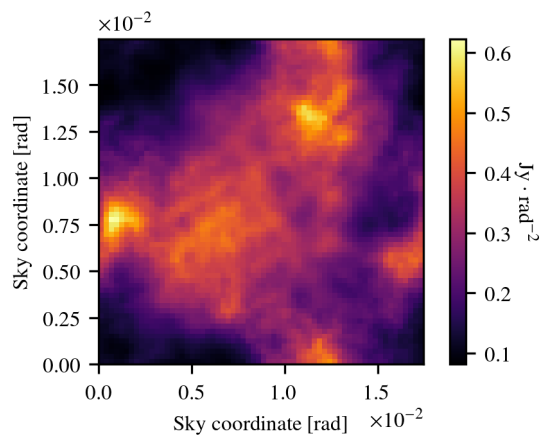


**Fig. 10.** Synthetic observation: pixel-wise standard deviation of posterior samples.

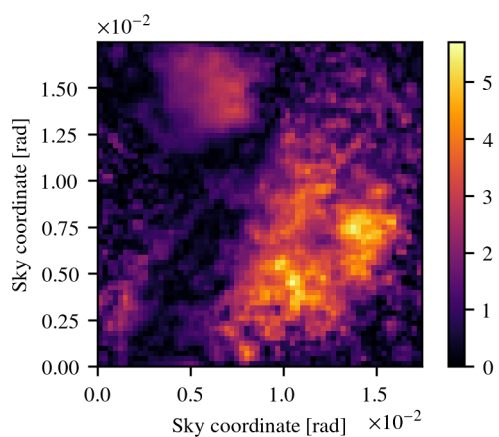


**Fig. 11.** Synthetic observation: absolute value of residual over pixel-wise standard deviation of posterior samples.

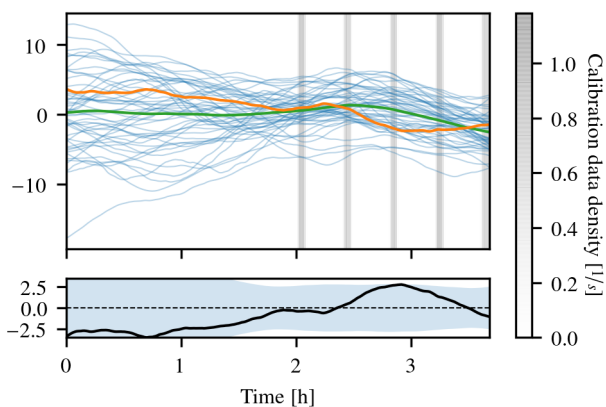


**Fig. 12.** Synthetic observation: phase solutions for antenna 15 and polarisation R. Colors as in Figure 13 and all phases are plotted in degrees. On the left-hand side all data points have been flagged.

#### 4. Application to VLA Data

Let us continue with an application of `RESOLVE` to real data. To this end, take the VLA data set whose uv-coverage and time stamps have already been used in the preceding section. It is a L-Band observation of the source G327.6+14.6, also known

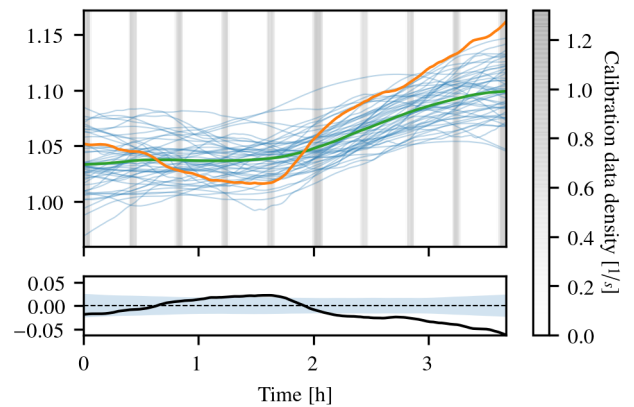


**Fig. 13.** Synthetic observation: amplitude solutions for antenna 0 and polarisation L. Orange: ground truth, green: sampled posterior mean, blue: posterior samples. The calibration data density shows how many data points of the calibrator observation are available. Note that a Bayesian algorithm can naturally deal with incomplete data or data from different sources. The lower plot shows the residual along with the pixel-wise posterior standard deviation.

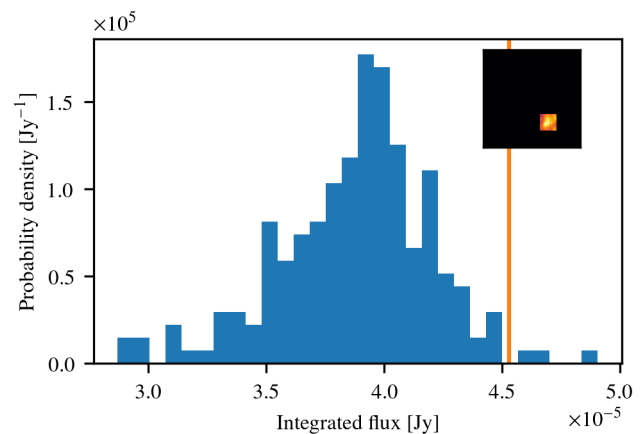


**Fig. 14.** Synthetic observation: histogram over samples of integrated flux in the region displayed in the upper right corner. Orange: Ground truth.

	$a$	$t_0$	$\bar{m}$	$\bar{y}$	$\sigma_m$	$\sigma_{y_0}$	$\alpha$	$\beta$
$A$	2	2	-4	2	1	2	4	1
$\lambda$	1.5	1	-4	-37	0.5	1	2	20
$\phi$	1.5	1	-4	-36	0.5	1	2	20

**Table 2.** SN1006: Prior parameters.

as SN1006. For the purpose of this paper we randomly select 30000 visibilities from this data set in order to demonstrate that joint calibration and imaging is possible even without much data. As before we use a resolution of  $64^2$  pixels at a field of view of  $60'$  and 256 temporal pixels for the calibration terms.

Starting from raw data, the first thing to look at, is the information source (see Figure 15). No structure of the supernova remnant is visible whatsoever since the data is not calibrated yet. This illustrates that `RESOLVE` is able to operate on raw (but already flagged) visibilities which have not been processed further. Table 2 summarizes the prior parameters for the following reconstruction.

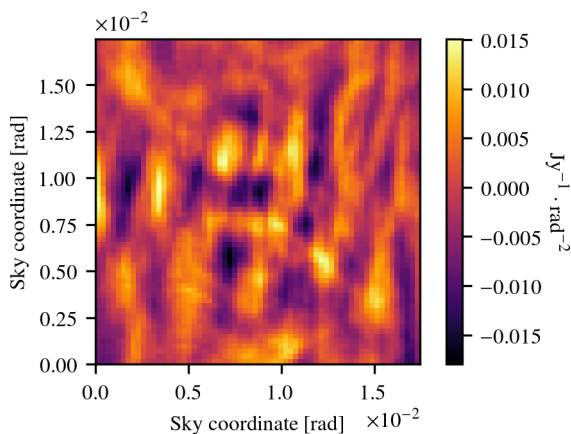


**Fig. 15.** SN1006: Information source  $j = R^\dagger N^{-1} d$ .

Let us analyze *RESOLVE*'s results. All calibration solutions are shown in Figure 16 together with two exemplary plots in Figures 17 and 18. The major characteristic of these solutions are hidden in the right-hand column of Figure 16: the uncertainty on the calibration goes down whenever the calibrator source is observed as expected. Additionally, the uncertainty increases dramatically where the data has been flagged. The amplitude solutions are surprisingly stable over time although the prior would allow for more variance in the solution as can be seen from Section 3, where the same prior parameters have been used.

There is a systematic difference between the samples for the amplitude solutions and the one for the phases. The first vary around a mean solution whereas the latter exhibit a certain global offset. This is explained by the fact that the likelihood is invariant under a pixel-wise global phase shift which is broken by the prior to a global phase shift to all temporal pixels at once. This residual symmetry is again broken by the prior on the zero-mode variance of the phase solutions. However, this prior is very weak in order to allow for phase solutions of arbitrary magnitude. Therefore, the phase solutions cannot have an arbitrarily large offset but still can globally vary to some degree which is what can be seen in Figure 18.

Next, the posterior sky brightness is discussed. Figures 19 and 20 accompanied by Figures 21 and 22 show the posterior mean and pixel-wise standard deviation of  $b(l, m)$ . The posterior standard deviation is higher wherever more flux is detected. Therefore, Figure 22 provides a descriptive visualization of the posterior uncertainty of the sky brightness distribution.

Last but not least also the power spectrum of the logarithmic sky brightness distribution needs to be reconstructed: it is shown in Figure 23. The power spectrum is more constrained compared to the one of section 3 since the noise level is much lower in this data set as compared to the synthetic data set.

All in all, this demonstrates that *RESOLVE* is not only able to operate on synthetic data but is actually capable of solving for the sky brightness distribution and the calibration terms at the same time for real data sets.

## 5. Conclusions

We have presented the probabilistic *RESOLVE* algorithm for simultaneous calibration and imaging. After a derivation from first principles of the full posterior probability distribution for the joint calibration and imaging algorithm *RESOLVE*, it has been shown how this distribution can be approximated by a multi-

variate Gaussian probability distribution in order to render the problem computationally solvable. This method is called Metric Gaussian Variational Inference (MGVI) and provides a prescription how to draw samples from the approximate posterior distribution. The calibration algorithm *RESOLVE* has been verified on synthetic data. The results indicate that the uncertainty quantification is sensible. However, they should be taken with a grain of salt since MGVI systematically underestimates posterior variance. Furthermore, it has been demonstrated that the algorithm has the capability to reconstruct a sky brightness distribution of an intricate source, the supernova remnant SN1006, together with uncertainty information from raw VLA L-Band data.

There are many open ends to continue the investigation which was started with this paper. First, the model for the sky brightness distribution may include point source and multi-frequency correlations. On top of that the response may be described more thoroughly. Direction-dependent calibration and non-trivial primary beam effects may be taken into account. Moreover, the flagging has been performed by a standard CASA flagging algorithm. One may replace this with an algorithm rooted in information theory which unifies flagging with calibration/imaging. Additionally, a major/minor cycle scheme similar to the one in CLEAN may be introduced in order to avoid frequent (de)gridding operations. This is necessary to apply *RESOLVE* to big data sets from telescopes like MeerKAT. Finally, one may extend *RESOLVE* to polarisation imaging.

On an orthogonal track *RESOLVE* may be used for imaging of a variety of sources from different telescopes including ALMA and especially the EHT.

*Acknowledgements.* We would like to thank Jamie Farnes for his workshop on calibration with CASA at the *Power of Faraday Tomography 2018* conference and his script for calibrating the data set at hand with CASA which enabled development of the IFT calibration algorithm, Landman Bester, Ben Hugo, Jakob Knollmüller, Julian Rüstig, Oleg Smirnov and Margret Westerkamp for numerous discussions, explanations and feedback, and Martin Reinecke for his work on NIFTY which was the crucial technical premise of the project. We acknowledge financial support by the German Federal Ministry of Education and Research (BMBF) under grant 05A17PB1 (Verbundprojekt D-MeerKAT).

## References

- Born, M. & Wolf, E. 1964, *E. 1964, Principles of Optics*  
 Cai, X., Pereyra, M., & McEwen, J. D. 2018, *Monthly Notices of the Royal Astronomical Society*, 480, 4154  
 Enßlin, T. A. 2018, *Annalen der Physik*, 1800127  
 Enßlin, T. A., Frommert, M., & Kitauro, F. S. 2009, *Physical Review D*, 80, 105005  
 Hamaker, J., Bregman, J., & Sault, R. 1996, *Astronomy and Astrophysics Supplement Series*, 117, 137  
 Högbom, J. 1974, *Astronomy and Astrophysics Supplement Series*, 15, 417  
 Hutschenreuter, S. & Enßlin, T. A. 2019, arXiv e-prints, arXiv:1903.06735  
 Junklewitz, H., Bell, M., Selig, M., & Enßlin, T. A. 2016, *Astronomy & Astrophysics*, 586, A76  
 Keiner, J., Kunis, S., & Potts, D. 2009, *ACM Transactions on Mathematical Software (TOMS)*, 36, 19  
 Kenyon, J., Smirnov, O., Grobler, T., & Perkins, S. 2018, *Monthly Notices of the Royal Astronomical Society*, 478, 2399  
 Khintchin, A. 1934, *Mathematische Annalen*, 109, 604  
 Knollmüller, J. & Enßlin, T. A. 2018, arXiv preprint arXiv:1812.04403  
 Knollmüller, J. & Enßlin, T. A. 2019, arXiv preprint arXiv:1901.11033  
 Knollmüller, J., Frank, P., & Enßlin, T. A. 2018, arXiv preprint arXiv:1804.05591  
 Leike, R. & Enßlin, T. 2019, arXiv preprint arXiv:1901.05971  
 Noordam, J. E. & Smirnov, O. M. 2010, *Astronomy & Astrophysics*, 524, A61  
 Offringa, A., McKinley, B., Hurley-Walker, N., et al. 2014, *Monthly Notices of the Royal Astronomical Society*, 444, 606  
 Perkins, S., Marais, P., Zwart, J., et al. 2015, *Astronomy and Computing*, 12, 73  
 Salvini, S. & Wijnholds, S. J. 2014, *Astronomy & Astrophysics*, 571, A97  
 Smirnov, O. M. 2011, *Astronomy & Astrophysics*, 527, A106  
 Thompson, A. R., Moran, J. M., Swenson, G. W., et al. 1986, *Interferometry and synthesis in radio astronomy* (Springer)  
 Wiener, N. 1949, *Extrapolation, interpolation, and smoothing of stationary time series*, Vol. 2 (MIT press Cambridge)  
 Wirtinger, W. 1927, *Mathematische Annalen*, 97, 357

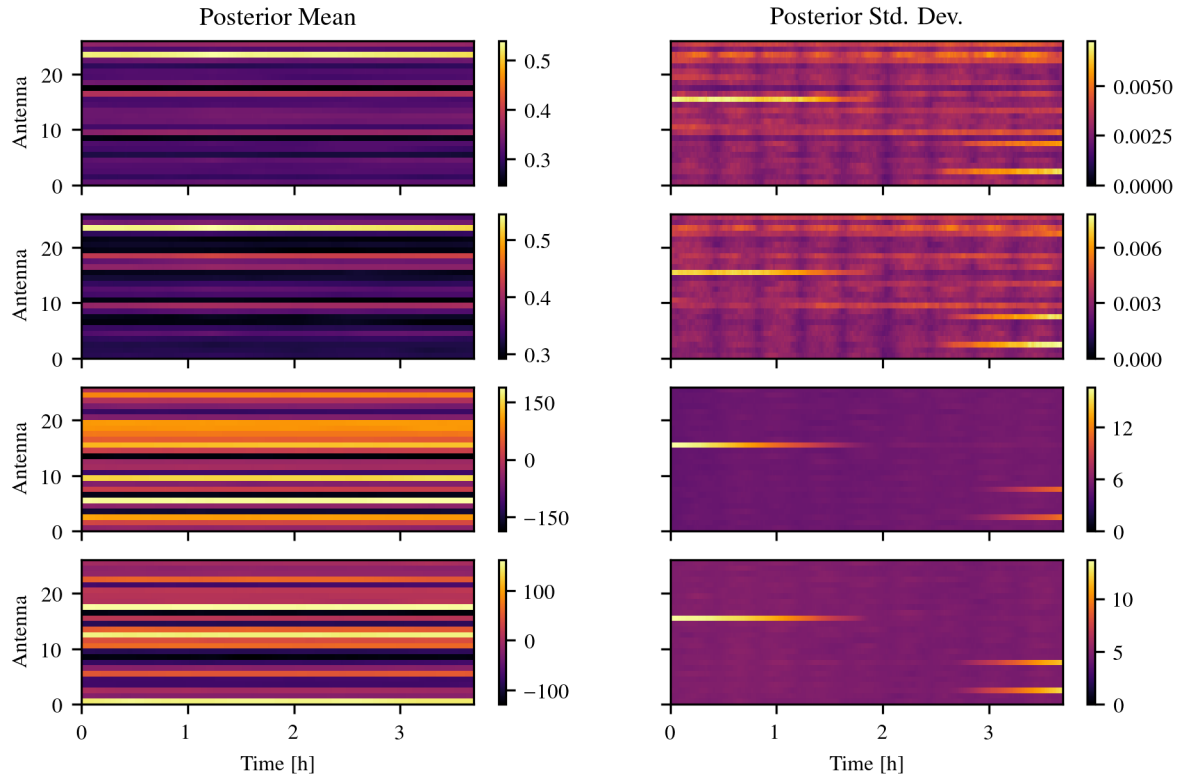


**Fig. 16.** SN1006: Overview over calibration solutions. The four rows indicate amplitude and phase solutions for LL- and RR-polarisation just like in Figure 7.

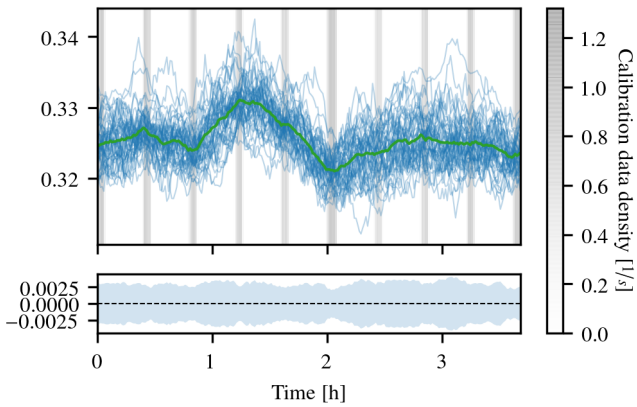


**Fig. 17.** SN1006: Exemplary amplitude solution (see Figure 13).

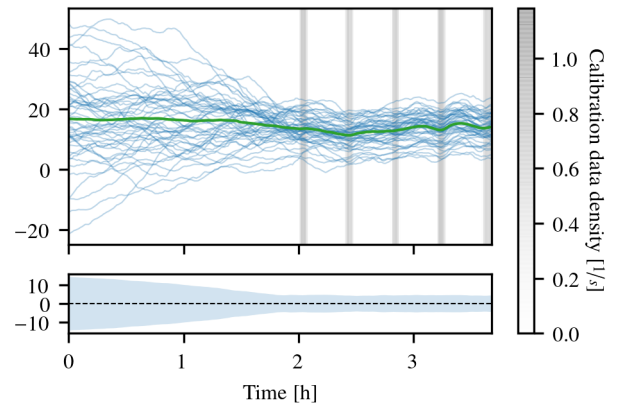


**Fig. 18.** SN1006: Exemplary phase solution (see Figure 12).

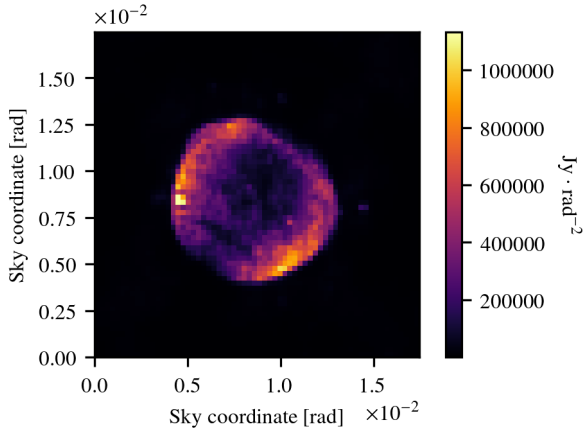


**Fig. 19.** SN1006: Sampled posterior mean of sky brightness distribution.

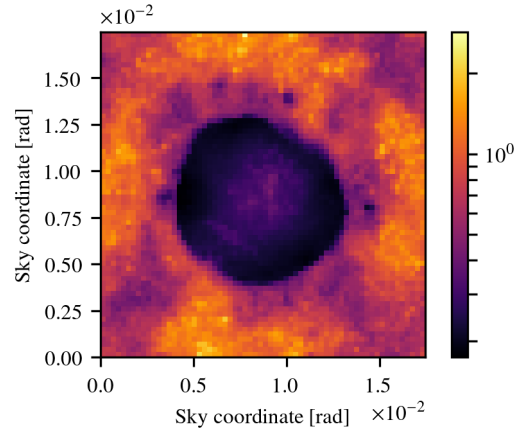


**Fig. 22.** SN1006: Pixel-wise posterior standard deviation normalized by posterior mean of sky brightness distribution.

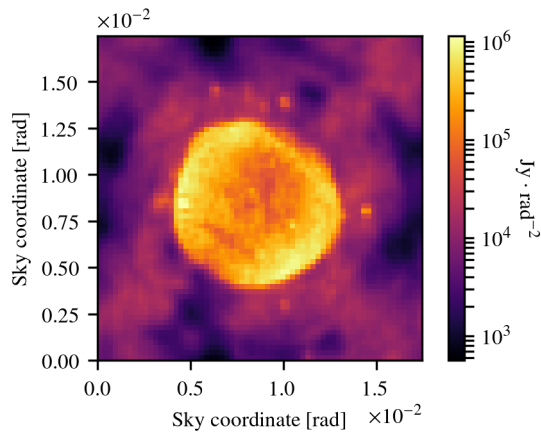


**Fig. 20.** SN1006: Sampled posterior mean of sky brightness distribution (logarithmic color bar).

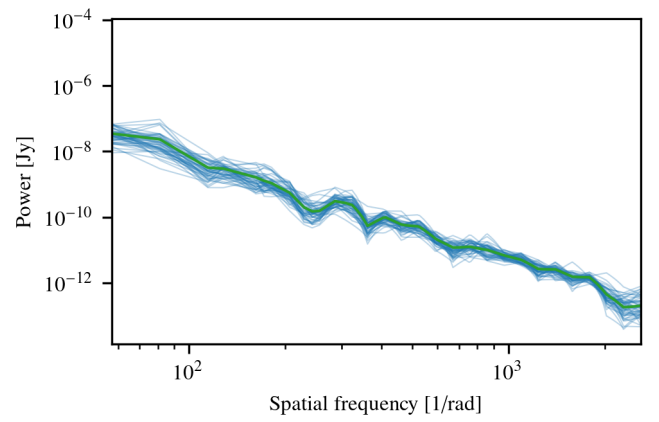


**Fig. 23.** SN1006: Posterior power spectrum of logarithmic sky brightness distribution.

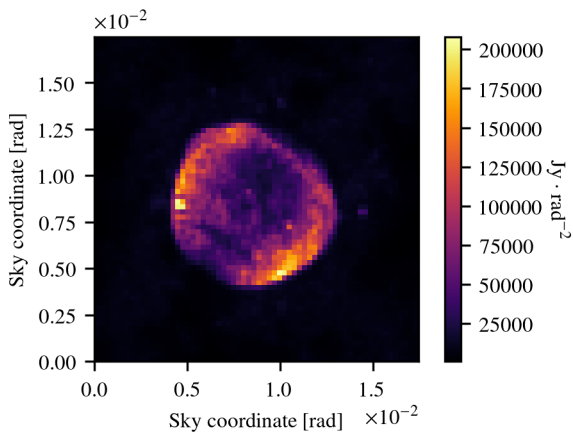


**Fig. 21.** SN1006: Pixel-wise posterior standard deviation of sky brightness distribution.